Refractive index-matched scanning of turbulent flows over rough permeable beds

Gauthier Rousseau, Christophe Ancey

Abstract

Measuring fluid velocity inside porous media is notoriously difficult, and this is why experimental investigations of fluid flow in porous media are seldom based on flow visualisation techniques. Here, we propose an experimental protocol that addresses this challenge. We show how using Particle Image Velocimetry (PIV) and a technique called Refractive Index-Matched Scanning (RIMS) makes it possible to measure fluid velocities in turbulent flows passing over permeable coarse-grained beds. As applications, we focused on supercritical shallow flows on steep slopes (in the 0.5%–8% range). In contrast with earlier PIV measurements using a fixed laser sheet, we scanned the flow across its width using a moving laser sheet. Recording fluid velocities continuously while translating the laser sheet allowed us not only to reconstruct the three-dimensional velocity and porosity field but also to reduce the amount of data requiring processing, and thereby the computational time. The reconstructions led to space- and time-averaged profiles as defined by the *double-averaging* procedure (Nikora *et al.*, *J. Hydr. Eng.* 127, 123-133, 2001). The present paper highlights the part that the bed layer's roughness played in the overall flow dynamics: the roughness layer is a buffer region in which turbulent stresses are rapidly dampened and porosity increases abruptly.

1 Introduction

Knowledge about how boundary-layer flows are affected by porous boundaries is central to many fluid applications, ranging from shear flows of air over and through forest canopies to heat transfer problems (Ghisalberti and Nepf, 2006). Open-channel flows over rough permeable beds are another case in point. Although these flows have been extensively studied (Nezu and Rodi, 1986; Nezu, 2005), there remain some unanswered questions. For instance, mountain rivers exhibit two distinctive features not shared by lowland rivers: (i) their flow-depth and roughness scales are similar which makes their turbulent structures far more complex; and (ii) their bed permeability is much higher. Both features help to explain why predicting flow resistance or the threshold of incipient motion is more complicated for mountain streams than for lowland rivers.

Making a grain-scale examination of the physical processes involved (see Fig. 1) reveals how bed protuberances act as obstacles to flow: they create local wakes, promote vorticity and produce different types of turbulent structures. As a result, turbulent boundary layers show large spatial heterogeneity (Mignot et al., 2009a). Flow paths—whether in the roughness or subsurface layer—are tortuous (these paths are sketched as dashed arrows in Fig. 1). All these elements make it impossible to use classic approaches to examining turbulence in shear flows (Keylock, 2015).

A fine-grained description of shallow turbulent flows over porous boundaries seems currently out of reach. However, this does not mean that we cannot gain any theoretical insight into the issue. Working at the mesoscopic scale, averaging flow properties over a control volume and taking their time averages makes it possible to provide a consistent physical picture of shallow turbulent flows. This approach relies on the *double-averaging concept* developed by Nikora et al. (2001, 2007) for turbulent boundary layers over rough permeable surfaces. In these cases, flow properties fluctuate in time and space. By averaging the Navier–Stokes equations over an appropriate timescale, then averaging the resulting equations over a thin control volume parallel to the bed surface, Nikora et al. (2007) derived the *double-averaged momentum equations*. This procedure is reminiscent of the Reynolds decomposition used for obtaining the Reynolds-averaged Navier–Stokes equations (RANS). As with the RANS equations, time-averaging produces the Reynolds tensor which is interpreted as the turbulent stress tensor. Additional terms arise when space-averaging the momentum balance equations: the *viscous drag*, the *pressure drag* and the *dispersive stress* (also termed the *form induced stress*). *Dispersive* and *turbulent stresses* are algebraically defined, and thus they can be determined from experiments or numerical simulations. *Dispersive stresses* are associated with the spatial variability of the velocity field, and their study is more delicate. Recent investigations have revealed that their contribution to the momentum balance is significant in heterogeneous flows (Voermans et al., 2017; Fang et al., 2018).

When double-averaging the mass and momentum balance equations for turbulent flows over porous boundaries, a new variable appears: the bed porosity. An additional equation is then needed to close the governing equations. One common assumption is that bed porosity is discontinuous: it jumps from a finite value to zero at the bed interface (Beavers and Joseph, 1967; Mendoza and Zhou, 1992; Breugem et al., 2006; Tilton and Cortelezzi, 2008; Rosti et al., 2015; Zampogna and Bottaro, 2016). This porosity jump is assumed to be associated with a momentum transfer at the bed interface (Ochoa-Tapia and Whitaker, 1995), whose strength is estimated by considering the Brinkman model; that is, a model describing how far a viscous stress is propagated through the porous medium (Brinkman, 1949). Using the Brinkman model is questionable, however, as there is no clear evidence that flow through the porous medium is dominated by viscosity when the surface layer is turbulent. In the absence of any experimental evidence of inertial exchanges between porous and surface flows, this question is still open. The lack of experimental evidence on this results from the difficulties of probing

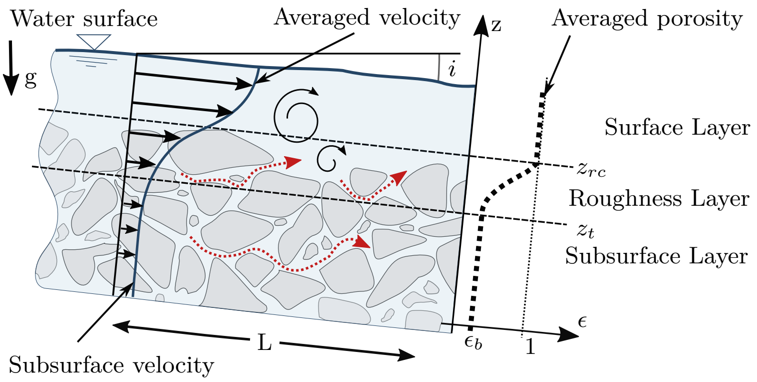

Figure 1: Grain-scale processes of a turbulent flow over a rough permeable bed. The porosity ϵ and velocity profiles are averaged over a thin layer parallel to the mean bed surface over the length L. The flow is subdivided into three specific regions: the *surface layer*, the *roughness layer* and the *subsurface layer*. The roughness layer is bounded by: (i) the roughness crest z_{rc} above which the averaged porosity is unity; and (ii) the troughs of the roughness elements z_t, where the bed porosity ϵ_b is reached. The red dotted arrows represent streamlines through the roughness and subsurface layers forming the permeable bed.

flow velocities without disturbing flows. Non-invasive methods such as *Particle Image Velocimetry* (PIV) or *Laser Doppler Velocimetry* (LDV) are of limited use because of bed opacity (Mignot et al., 2009a; Cameron et al., 2017; **?**). Authors such as Pokrajac and Manes (2009) created artificial porous beds that enabled the visualisation of subsurface flows through the flume's sidewall, but these bed structures are far removed from real-world beds.

This article presents an experimental procedure for investigating turbulent flows over and through a porous coarse-grained bed in low relative-submergence conditions, i.e. grains at the surface of the bed are similar in size to the flow depth. Further physical insights into flow behaviour are provided by using the *double averaging* approach. This approach focuses on determining the porosity and velocity profiles as well as the dispersive and turbulent stresses present at the mesoscopic scale, that is, at a large length-scale in comparison to the roughness size. This paper is innovative because it couples the *Refractive Index-Matched Scanning* (RIMS) method with a PIV technique to measure flow velocities over and through the porous bed. RIMS is an interesting technique, which involves matching the fluid's and the beads' refractive indices—so that the mixture becomes transparent (see Fig. 2)—and scanning the mixture using a moving laser sheet (MLS) (**?**Ni and Capart, 2015; van der Vaart et al., 2015). In a similar fashion to ours, Voermans et al. (2017) used an index matching technique to study mass and momentum transfers across the interface between the surface and subsurface flows, although flows remained subcritical with high relative-submergence conditions. Our experiments measured velocities continuously using a laser sheet mounted on a linear unit moving in the transverse direction. This enabled us to reconstruct velocities within the entire volume monitored using a high-speed camera.

The article is organised as follows: Section 2 describes the experimental setup and protocol used in our experiments. Section 3 describes the scanning procedure used to determine flow properties at the mesoscopic scale. We show that this procedure imposed constraints on the scanning rate. Section 4 focuses on data reproducibility and uncertainties.

2 Experimental setup

2.1 Flume and materials

The experiments were performed in a 6-cm wide, 2.5-m long flume with an adjustable slope i, as shown in Figure 3. A constant head tank provided a steady fluid discharge into the system. Equal proportions of borosilicate beads of two diameters (7 and 9 mm) were randomly packed into the flume bottom, forming the coarse-grained bed. The mean particle diameter was thus $d_{50} = 8$ mm. A bed composed of beads of the same diameter would arrange itself in parallel layers causing undesirable bias in the averaged porosity and velocity profiles. Before each run, the upper layer was flattened out to form a uniform bed of height $h_s = 5$ cm. Flow disturbances at the flume inlet were reduced using straighteners, and the region of interest (ROI—where measurements were made) was located far upstream of the permeable grid placed at the flume outlet to maintain the beads while letting the flow seep out of the bed. Even though surface flows were supercritical, the downstream condition at the flume outlet affected the flow dynamics. For example, if the grid had been replaced with an impermeable wall, a dead zone would have appeared in the bed just upstream of the wall, causing flow resurgence and changes to the surface flow. Despite this measure, we could not exclude the development of substantial pore-pressure variations near the

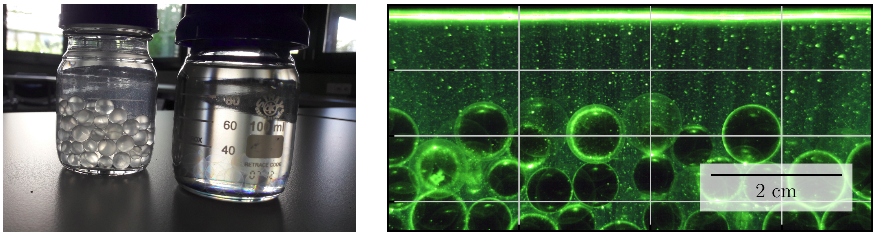

Figure 2: Left: Two beakers containing equal quantities of borosilicate beads representing the porous bed. The left-hand beaker contains water and the refractive index mismatch means that the beads are visible; the right-hand beaker contains a fluid whose refractive index matches that of the beads, rendering them invisible, but the interstitial fluid can be probed using flow visualisation techniques. Right: Photograph of a gravity-driven flow (on a $i = 0.5\%$ slope) over a porous bed made of the same borosilicate beads. The RIMS technique enables us to visualise the interior of the roughness and subsurface layers: the black disks are the borosilicate beads illuminated by the laser sheet, whereas the small dots are tracers. A PIV technique was used to measure the flow velocity.

flume outlet. This problem is discussed in Section 4.3.

The iso-index fluid was prepared by mixing volumic concentrations of 40% ethanol and 60% benzyl alcohol. The refractive index n_f of the resulting fluid matched that of the borosilicate beads. Using a digital refractometer (ATAGO RX-5000 α), we found $n_f = n_{borosilicate-glass} = 1.472 \pm 0.002$ at 20°C. The iso-index fluid's physicochemical characteristics were close to those of water. Using a Cannon-Ubbelhode viscosimeter, we measured its kinematic viscosity at a temperature of 20°C: $\nu_f = 3.0 \pm 0.1$ mP·s. Its density was $\rho_f = 950 \pm 10$ kg·m^{-3} (details of these measurements are provided in Rousseau (2019) - Annex D). These values were close to those obtained by Chen et al. (2012). According to these authors, surface tension was about $\sigma_f = 31 \pm 1$ mN · m^{-1}, which is a factor of 2 lower than that of water. Surface tension was thus assumed to have negligible effects on our experimental flow dynamics. The borosilicate beads' density was $\rho_s = 2200$ kg·m^{-3}. Compared to other materials used in RIMS techniques, combining borosilicate, ethanol and benzyl alcohol leads to mixtures whose relative density is close to that found in real-world scenarios like river engineering. Meeting these similarity criteria (e.g. the Shields and Froude numbers) is necessary to obtain flow conditions that mimic those encountered in real-world scenarios (e.g. a shallow flow on a steep slope with a low sediment transport rate, such as mountain streams). If we had followed Ni and Capart (2015) and used a sediment of poly(methyl methacrylate), with a density of $\rho_s = 1190$ kg·m^{-3}, it would have been impossible to conduct experiments on steep slopes without observing sediment transport. The same observations would be expected when employing a popular RIMS fluid mixture made of NaI (e.g. as in Voermans et al. (2017)) since, in this case, the fluid has an unexpectedly high density: $\rho_{f,\mathrm{NaI}} = 1770 \pm 10$ kg·m^{-3}. In the present context, we needed a stable bed which could resist the stream's erosive action when the flow reached supercritical states.

The iso-index fluid was initially contained in a reservoir (with a volume of about 10 L) connected to a second reservoir below it where an overflow pipe kept the fluid depth constant, ensuring a steady flow rate into the flume. Two valves controlled the desired flow rate: the first valve was manually controlled and regulated the base flow. The second was driven by an electro-valve and was used to adjust the flow rate to the desired value q_f. As shown in Fig. 3-(a), the reservoir was fixed at the flume's upstream end to obtain constant pressure heads regardless of the flume inclination. As the inclination did not exceed 8%, it had a negligible influence on the pressure head. Uncertainties on the flow rate were lower than 5%.

The iso-index fluid was chemically stable. At the interface between the flow and air, ethanol evaporated, a problem which might affect the fluid's refractive index in the long run. Ethanol was thus added whenever needed. The refractive index matching value n_f was controlled between two consecutive runs. Small quantities of a fluorescent dye (Rhodamine B) were added to the fluid to increase the contrast between the beads and fluid. Our laboratory had previously used this combination of borosilicate beads and Rhodamine B to determine bead positions in three-dimensional experiments on particle segregation in granular flows (van der Vaart et al., 2015).

2.2 Optical system

Frame sequences were recorded using a Basler acA2040-180kc camera operated at a rate of 420 frames per second and a resolution of 1496 × 700 pixels (px). The lens' focal length was 35 mm and the aperture was $f/2.8$. The camera was placed 30 cm from the sidewall, giving a field of vision of 73.8×34.5 mm^2. Thus, the mesoscopic scale L over which spatial averaging was performed was about 8 cm or ten bead diameters. The flow was seeded with micrometric PIV tracers (hollow glass spheres 8–12 μm in diameter). The tracers were lit up by a 4 W diode-pumped solid-state laser (emitting at 532 nm) mounted on a linear unit. The laser sheet's

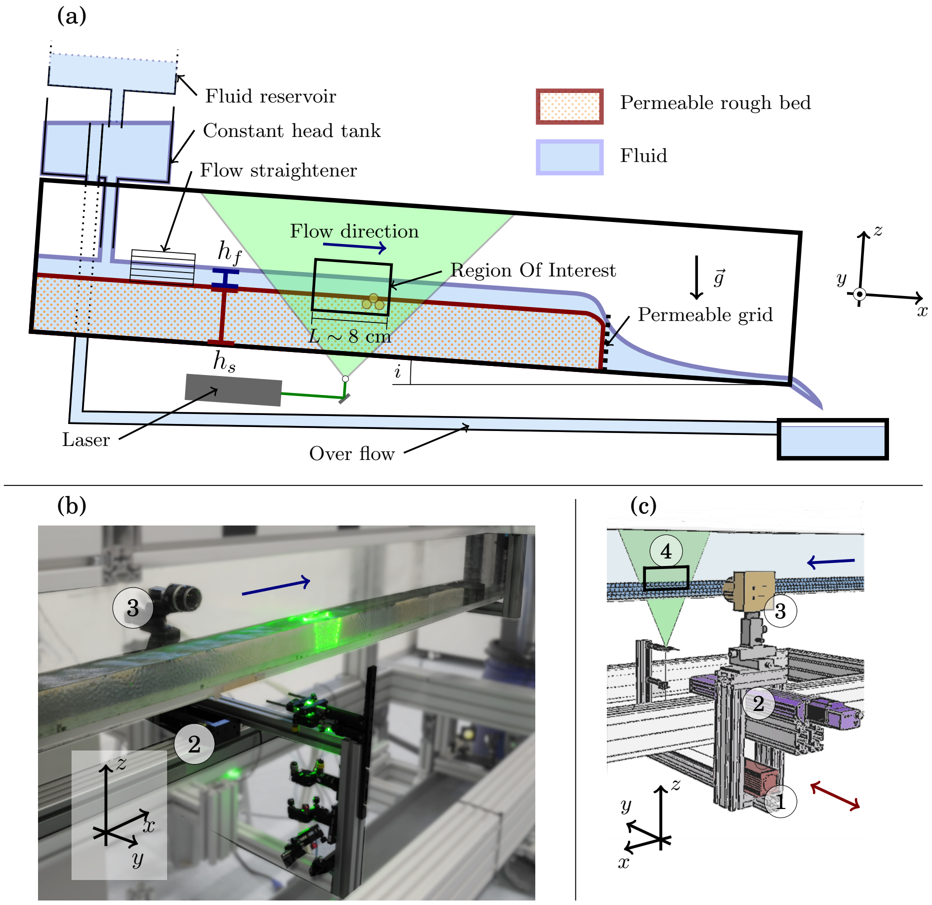

Figure 3: (a) Sketch of the experimental set-up. (b) Photograph of the flume. (c) Three-dimensional visualisation sketch. 1 laser; 2 linear unit for displacement along the y-axis; 3 high-speed camera; 4 laser sheet.

linear movement perpendicular to the flow enabled us to scan the ROI by taking images from the flume's sidewall.

2.3 Transverse scanning and porosity profiles

Shifting the laser along the y-axis made it possible to take images in parallel planes and thus infer bead positions $(x_b,\, y_b,\, z_b)_n$ and diameters D_n. After determining the bead positions, we built up a three-dimensional matrix of the porosity $B(x_i,\, y_j,\, z_k)$ $(1 \leq i \leq M$, $1 \leq j \leq N$, and $1 \leq k \leq K)$ for the ROI, with a resolution of approximately one tenth of a bead diameter. This porosity array generalised the *roughness geometry function* defined by Nikora et al. (2001)). Each entry took the value of 0 if the datapoint $(x,\, y,\, z)$ lay in a bead and 1 if it did not. When the point was close to the bead–fluid interface, the entry took a value ranging from 0 to 1 representing the volume-averaged porosity of the cell centred at $(x,\, y,\, z)$. We then obtained the averaged porosity for a slice of the porous bed at a position y on the laser sheet by summing the array over i and then dividing by the window length. The discrete spatial averaging was defined by:

$$\epsilon(z_k|y_j) = \frac{1}{M}\sum_{x_0}^{x_M} B(x_i,\, y_j,\, z_k).$$

Similarly, we defined a cross-stream-averaged porosity profile by averaging B in the x- and y-directions (see Figure 4):

$$\epsilon(z_k) = \frac{1}{MN}\sum_{i}^{M}\sum_{j}^{N} B(x_i,\, y_j,\, z_k).$$

The time-and-space-averaged depth was defined by:

$$h_f = \left\langle \overline{z_{surf}(x,\, t) - z_b} \right\rangle,$$

where z_{surf} is the free-surface position and z_b is the bed level. For low relative-submergence flow conditions, i.e. for $S_m = h_f/d_p \sim 1$, a definition of z_b is essential. This quantity is used to deduce important flow parameters such as flow depth h_f and, in consequence, the bed shear stress $(\tau_b = \rho_f g h_f \sin(\theta))$. A slight change in the

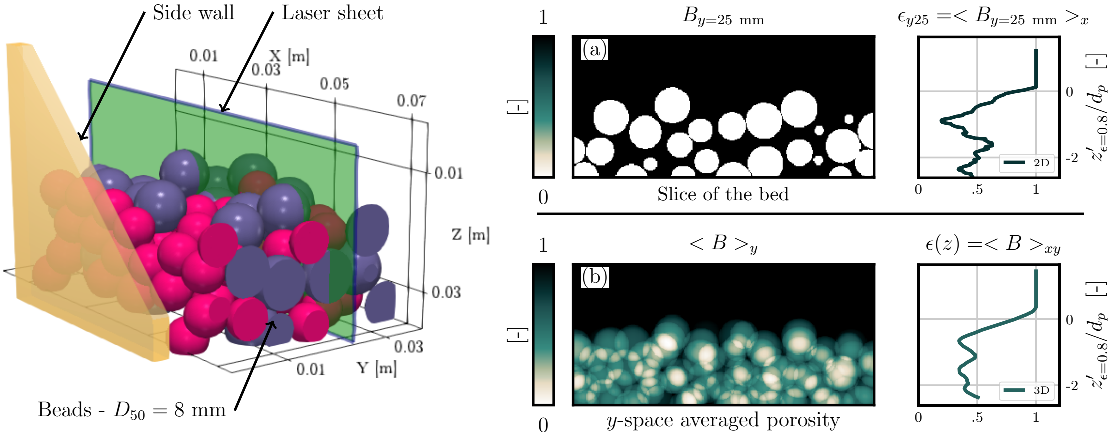

Figure 4: Porosity measurement using RIMS: once the beads have been located, we define the porosity array $B(x, y, z)$. (a) The B field averaged in the x-direction in a slice located at $Y_m = y - y_w = 25$ mm from the wall position y_w. (b) Averaging B over x and y gives us a smooth porosity profile. The relative vertical coordinate is denoted by $z'_{\epsilon=0.8} = z - z_b$ and is computed from z_b, which is the vertical coordinate for which bed porosity is 0.8.

definition may significantly alter these flow characteristics and the interpretation of the results, as highlighted by Pokrajac and Manes (2009).

Here, z_b was defined at $z(\epsilon = 0.8)$, which is the vertical coordinate where porosity is equal to 0.8 (). This gave a z_b slightly below the roughness crest z_{rc}. As there is no consensus about the definition of z_b for rough beds, this choice might seem arbitrary, but it had the advantage of providing consistent profiles when bed arrangement was changed. We take a closer look at the issue of this choice in Section 4.2. In the following sections, the vertical coordinate is always referred to as the bed level, i.e. $z'_{\epsilon=0.8} = z - z_b$.

3 Velocimetry and transverse scans

3.1 Image velocimetry processing

The selection of an appropriate image processing technique for our experiments was constrained by two factors: (i) we estimated that the fluid passing through our roughness layer would exhibit substantial velocity variations; and (ii) we knew the gaps between the beads were narrow. These features would require the use of image velocimetry tools able to function across a sizeable dynamic range. We tested different methods, from classic PIV to the more elaborate particle tracking velocimetry (PTV). The open-source Python library, *openCV*, was the best suited to our needs.

The algorithm measures the local *optical flow* by means of a pyramidal application of the Lukas–Kanade method (Bouguet, 2001). The optical flow method obtains the displacement field by minimising the squared *Displaced Frame Difference* (DFD). The methodology is similar to that of PIV algorithms, but it is optimised to be able to extract the displacement of any feature. Indeed, in classic PIV, algorithms are optimised for measuring particle displacement. For a better sense of the equations underpinning the algorithm, and its difference from classic PIV, the reader is referred to Liu and Shen (2008); Heitz et al. (2010); Boutier (2012). In turbulence, this methodology was used by Miozzi et al. (2008) and more recently by Zhang and Chanson (2018). Appendix A provides further information on the image velocimetry techniques used in our experiments. This appendix includes a test on the Case-A proposed in the 4th PIV challenge (Kähler et al., 2016). The algorithms showing the test results are all available from the public GitHub repository: `https://github.com/groussea/opyflow`.

3.2 Quantities of interest within the double-averaging framework

Turbulent flows over rough permeable beds exhibit strong spatial and temporal variability. The *double-averaging* concept was developed to cope with flow variability (Nikora et al., 2007). We consider a steady uniform flow and seek to define its mesoscopic flow properties. Step 1 involves using the generalised Reynolds decomposition by breaking down the local instantaneous velocity into the time–space averaged value $\langle \overline{u_k} \rangle$ (with $k = x$, y or z), the local disturbance $\widetilde{u}_k$ and the temporal fluctuations u'_k in the three spatial directions. For a two-dimensional open-channel flow, the *double-averaged decomposition* gives:

$$\boldsymbol{V(x, y, z, t)} = \begin{bmatrix} u_x \\ u_y \\ u_z \end{bmatrix} = \begin{bmatrix} \langle \overline{u_x} \rangle + \widetilde{u}_x + u'_x \\ \widetilde{u}_y + u'_y \\ \widetilde{u}_z + u'_z \end{bmatrix}. \quad (1)$$

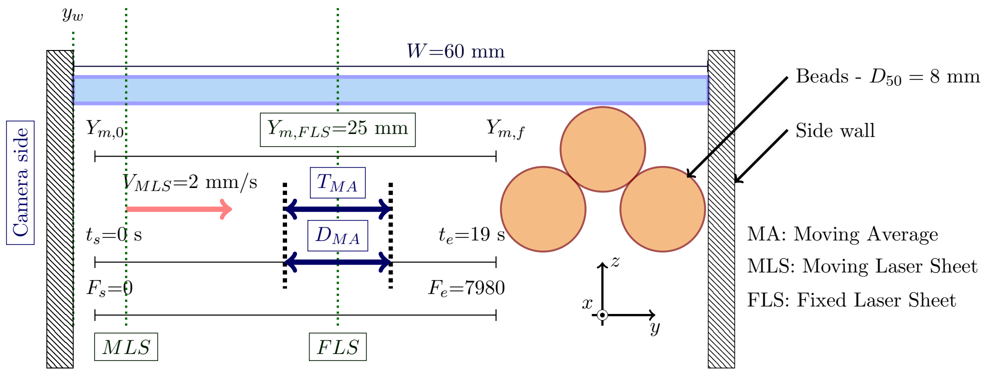

Figure 5: Schema of the transverse scanning set up and comparison with a fixed laser sheet (FLS) measurement. Fs and Fe are the start and end frame indexes, respectively.

The superscript $\overline{\bullet}$ represents time averaging, the brackets $\langle\bullet\rangle$ are the intrinsic space averaging (i.e. over the fluid phase only) and the tilde superscript $\tilde{\bullet}$ denotes the local spatial disturbance. The control volume's dimensions in the x- and y-directions are sufficiently large for the mean fluctuating velocities $\langle\widetilde{u}_x\rangle$, $\langle\widetilde{u}_y\rangle$ and $\langle\widetilde{u}_z\rangle$ to be negligibly small. *Double-averaging* the Navier–Stokes equations produces the double-averaged momentum equations, whose projection on the streamwise x-direction is (Nikora et al., 2001):

$$0 = \epsilon\rho_f g i + \frac{\mathrm{d}\tau_d}{\mathrm{d}z} + \frac{\mathrm{d}\tau_t}{\mathrm{d}z} + \frac{\mathrm{d}\tau_v}{\mathrm{d}z} + f_{p,x} + f_{v,x}, \qquad (2)$$

where $\tau_d = -\rho_f\epsilon\langle\widetilde{u}_x\widetilde{u}_z\rangle$ and $\tau_t = -\rho_f\epsilon\langle\overline{u'_x u'_z}\rangle$ are called the *dispersive* (or *form induced*) and *turbulent* stresses, respectively. $f_{p,x}$ and $f_{v,x}$ are called the *pressure drag* and *viscous drag* on the solid element surfaces. τ_v is the viscous stress.

Here, the turbulent stress τ_t and the dispersive stress τ_d have to be estimated from experiments. To that end, we must first measure the spatial disturbances ($\tilde{u}_x$,$\tilde{u}_x$) and the fluctuations (u'_x,u'_z) in a specific ROI.

The velocity disturbance at any position can be estimated as $\tilde{u}_i = \overline{u_i}(x,y,z) - \langle\overline{u_i}\rangle$, where $u_i(x,y,z,t)$ denotes the instantaneous local velocity in the i-direction, $\overline{u_i}(x,y,z)$ is the local time averaged velocity and $\langle\overline{u_i}\rangle$ is the double-averaged velocity in a thin layer parallel to the mean bed surface at the mesoscopic scale. In the x-direction, we have $U_x = \langle\overline{u_x}\rangle$, and if the flow is unidirectional at the mesoscopic scale, we also have $\langle\overline{u_y}\rangle = \langle\overline{u_z}\rangle = 0$. A necessary condition for the flow to be considered two-dimensional is that these equations can be verified experimentally, and that the flow depth is uniform in the x- and y-directions. For further information on the fundamentals of *double-averaging*, the reader is referred to (Nikora et al., 2007).

In the surface layer (i.e. for $z > z_{rc}$ where $\epsilon(z) = 1$), the *double-averaged momentum equation* is:

$$0 = \rho_f g(h - z)\sin\zeta + \tau_t + \tau_d + \tau_v. \qquad (3)$$

In the permeable bed below the roughness crest (i.e. for $\epsilon(z) < 1$), these assumptions are no longer valid because of drag interactions.

3.3 Constraints on laser sheet displacement when measuring using scanning

Section 2.3 presented the scanning methodology used to detect bead positions and acquire porosity profiles. Fluid velocity measurements can also be collected during the laser sheet displacement. Although this choice has the advantage of reducing data storage and experiment duration, it imposes constraints on the cart velocity because of the spatial and temporal heterogeneity of the flow. The first constraint is related to the limitations of the camera's acquisition rate: if the cart moves faster than this limit, it is impossible to take the pairs of images required by PIV methods for measuring the velocity field. The second constraint is imposed by turbulence: the time during which the camera monitors a given flow slice must be sufficiently long to obtain accurate estimates of turbulence statistics, e.g. for estimating local turbulent stress. With reference to the graphical representation of the scanning procedure given in Figure 5, these two conditions can be expressed as follows:

- With a laser sheet moving in the transversal direction at a constant velocity V_{MLS} (MLS), the local fluid velocities measured during the translation depend on the flow's length scale L_u, which in turn depends on the spatial variations in the bed topography. Thus, taking measurements at a frame acquisition rate f must meet the following condition:

$$V_{MLS} < fL_u. \qquad (4)$$

- As the local information fluctuates with time, we have to wait for a period $T_{u'}$ to determine the local turbulence statistics (average and standard deviation). This affects the measurement strategy significantly by imposing the second constraint:

$$V_{MLS} < L_u / T_{u'}. \quad (5)$$

Because no preliminary information was available on the characteristic turbulent time $T_{u'}$, experiments must estimate its order of magnitude. Section § 3.5 tackles this issue. The next section outlines the averaging procedures.

3.4 Scanning and averaging procedure

Once the laser sheet has been shifted, time averaging is defined as:

$$\overline{\theta}_{Tm,T_{MA}} = \frac{1}{T_{MA}} \int_{T_m - T_{MA}/2}^{T_m + T_{MA}/2} \theta(y_l(t)) \mathrm{d}t \quad (6)$$

where θ is any local quantity of interest, such as the velocity $u_x(t, x, y_l, z)$ or the instantaneous shear stress $\rho\, u'_x u'_z(t, x, y_l, z)$. Time T_{MA} is the moving-average time, that is, the time window over which time averaging is done to obtain average local flow and turbulence statistics. Measurement is made at time T_m, and thus the time window is centred on it. We denote the laser sheet's position by $y_l(t)$: $y_l = V_{MLS}\, t + y_0$, where y_0 is its position at $t = 0$.

Time-averages are then space-averaged over the y-axis. Averaging over the period T_{MA} at time $T_m = Y_m / V_{MLS}$ implies that the averaging is done over the length $D_{MA} = V_{MLS}\, T_{MA}$ around Y_m (see Fig. 5). The following condition is then obtained by matching the time- and space-averaging:

$$\overline{\theta}_{Tm,T_{MA}} = \langle \theta \rangle_{Y_m, D_{MA}} = \frac{1}{D_{MA}} \int_{Y_m - D_{MA}/2}^{Y_m + D_{MA}/2} \theta(y_l(t)) \mathrm{d}y_l. \quad (7)$$

Note that there is only one measurement at time t and at position y_l during the translation. As the laser sheet has a finite thickness (about 1 mm), this thickness has to be included in the length D_{MA}. When using RIMS techniques, time and space dependencies are intertwined, and it is therefore crucial to check the procedure's reliability with great care by comparing the RIMS measurements with those obtained using an FLS at Y_m over a long time period.

3.5 Evaluation of the scanning methodology

3.5.1 Flow characteristics and evaluation procedure

To assess scanning performance, we conducted two runs using the hydraulic characteristics detailed in Table 1. The bed arrangement was the same in both runs, but the runs differed as follows:

- In the first run, velocities were obtained using PIV and an FLS positioned at $Y_{m,FLS} = 25$ mm.
- In the second run, velocities were obtained using the PIV–RIMS methodology and the flume was scanned using an MLS sheet from $Y_{m,0} = 2$ mm to $Y_{m,f} = 40$ mm.

First, we estimated the lag time $T_{u'}$ required to obtain accurate time-averaged quantities from the FLS measurements. A 20-s period gave a robust estimate of the turbulence statistics near protuberances, making it possible to estimate $T_{u'}$. The velocity of the MLS V_{MLS} could then be deduced from the constraints imposed by Eq. (4) and Eq. (5). Scanning performance was evaluated by comparing the mean velocities and turbulent stresses obtained using the RIMS methodology and those obtained by the FLS. Table 2 summarises these results.

3.5.2 Temporal and spatial averaging measurements using the fixed laser sheet

Figure 7 shows a snapshot of the vertical and horizontal velocity components, their time-averaged fields, and the resulting space- and time-averaged velocity profiles with the laser sheet fixed at $Y_m = 25$ cm. The light green areas give an idea of the spatial variability of the time-averaged velocities. The same is then done for the velocity fluctuations, disturbances and turbulent stresses.

The time-averaged vertical velocity field $\overline{u_z}$ helps to understand why spatial averaging is useful (see Fig. 7 – (b2)): $\overline{u_z}$ exhibited large spatial variability. At this local scale, the flow was neither uniform nor unidirectional. It was only at the mesoscopic scale, after appropriate space-averaging, that the flow could be considered uniform and unidirectional. As shown by Figure 7 – (b3), the space-averaged vertical velocity profile $\langle \overline{u_z} \rangle$ was close to zero across the entire depth, confirming flow uniformity.

The time-averaged turbulence intensities along x and z also showed substantial spatial variability (see Figs. 7(c2) and (d2)). Zones of high $\overline{|u'_x|}$ values were observed behind protuberances due to their generation of turbulent wakes. $\overline{|u'_z|}$ remained more homogeneous, but its magnitude was higher, not only in the turbulent wakes but also against bead front faces on top of the bed. Inside the permeable bed, the turbulent activity was negligibly small. This observation must be tempered owing to the errors made when measuring small velocities using PIV. Indeed, we had $\Delta\overline{|u'_i|}_{small} \pm 2$ mm/s. The highest velocities at the free surface were similarly subject to greater inaccuracy owing to the difficulties in measuring displacements at the surface (see Fig. 7 – (c3,d3)). If vertical turbulence intensities were assumed to be zero at the free surface, then the observed fluctuation might have resulted from the inaccuracy at this elevation as we had $\Delta\overline{|u'_i|}_{high} \pm 5$ mm/s.

We found that the turbulent stress τ_t roughly matched the depth-averaged momentum flux, as expected from the momentum balance equation (3) when the dispersive and viscous stresses can be neglected

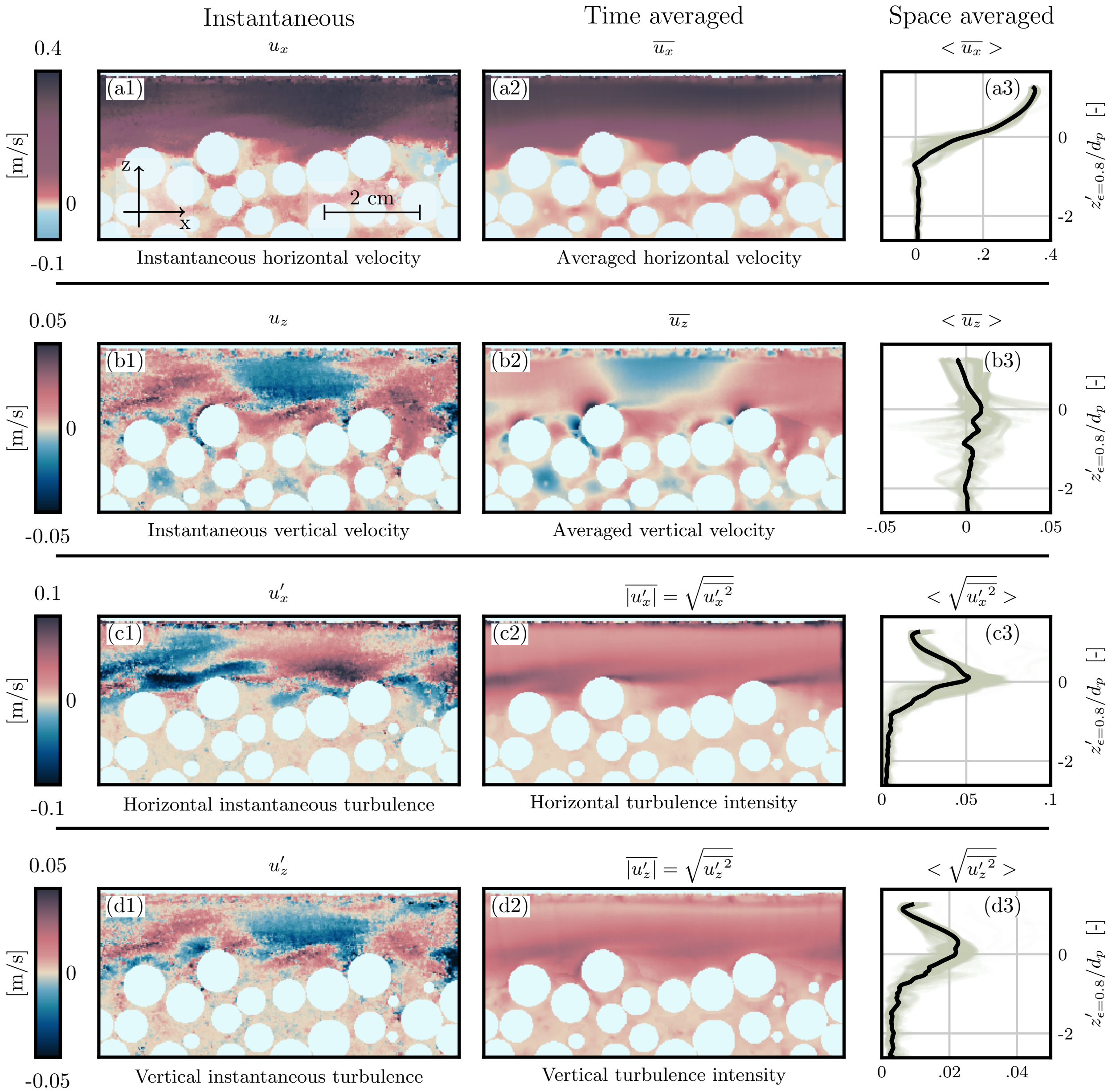

Figure 6: From instantaneous to *double-averaged* quantities. In this configuration, the laser sheet was fixed at a position $Y_m = 25$ mm from the side wall and it recorded the flow for 20 s. Instantaneous measurements were selected randomly, but each measurement is shown for the same moment during those 20 seconds. From the top to the bottom, the images show the horizontal and vertical averaged velocities and the horizontal and vertical turbulence intensities.

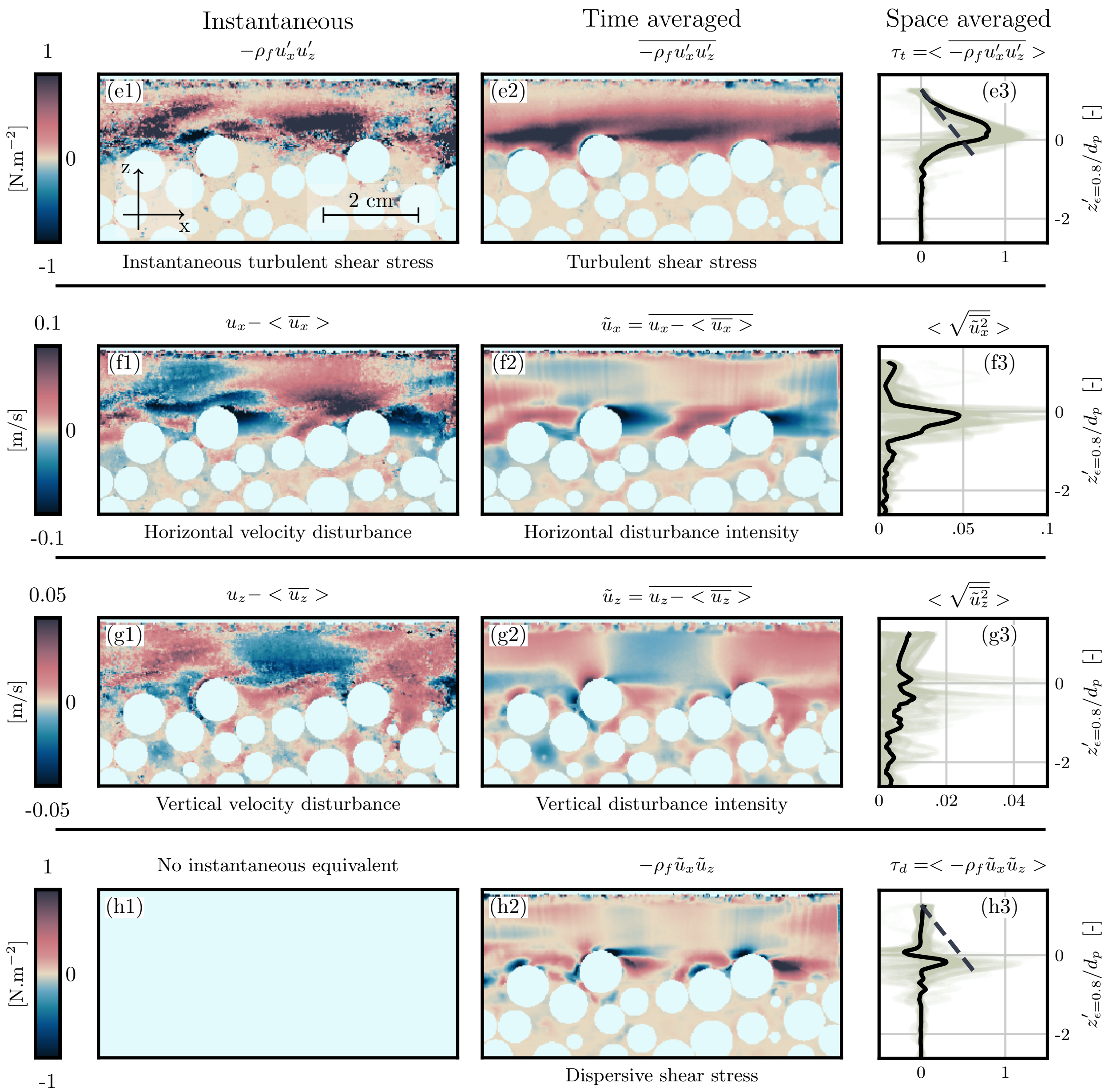

Figure 7: From instantaneous to *double-averaged* quantities with conditions similar to Figure 6. From the top to the bottom, the images show turbulent stresses, the horizontal and vertical disturbances and the dispersive stresses. Dotted lines show the integrated gravity from the surface elevation $\rho\, g\, (z_{surf} - z)\, i$.

i	W [cm]	Q [mL/s]	q_f [$\times$ 10^3 m^2/s]	h_f [mm]	U_{surf} [m/s]
0.5%	6.0	182	3.0	11	0.34

U_b	Re_b	Fr	U_{SSL} [m/s]	d_{50} [mm]	Re_{SSL}	S_m [-]
0.28	1026	1.04	0.015	8	41	1.35

Table 1: Experimental conditions for testing the PIV–RIMS methodology: U_{surf} is the surface velocity, $Re_b = U_b h/\nu$ is the surface Reynolds number, $Fr = U_{surf}/\sqrt{gh}$ is the Froude number, U_{SSL} is the mean subsurface layer velocity, $Re_{SSL} = d_{50}U_i/\nu$ is the interstitial Reynolds number and $S_m = h_f/d_{50}$ is the relative submergence.

	Type	Y_m [mm]	T_{tot} [s]	f	V_{MLS} [m·s^{-1}]
Case 1	Fixed Laser Sheet (FLS)	25	20	210	0
Case 2	Moving Laser Sheet (MLS)	2 – 40	20	210	0.002

Table 2: Experimental conditions for the Fixed Laser Sheet and the Moving Laser Sheet.

inside the surface layer. The spatial disturbance fields $\tilde{u}_z$ and $\tilde{u}_x$ also exhibited large spatial variability (see Figs. 7 − (f2,g2)), but contrary to the turbulence intensities, their peak values were observed around the beads rather than in their wakes. Note that the spatial disturbance could be positive or negative, which was not the case for the turbulence intensities. As observed in Fig. 7(f2), there were small zones in front of and behind beads where the horizontal velocity components were lower. In these zones, vertical velocity was more often oriented upward. As a result, the dispersive stress $\tau_d = \langle -\rho_f \tilde{u}_x \tilde{u}_z \rangle$ was more often positive than negative at the interface (see Fig. 7-(h3)). For the FLS setting, measurement was made in a single flow slice, and the dispersive stress was negative on top of the bed. This feature was not observed when averaging a larger domain using the PIV–RIMS procedure, as shown in Section 5.1.1. The dispersive stress affected both the front and rear of protuberances, i.e. where the *velocity deficit* was significant (see Fig. 7(h2)).

3.5.3 Turbulence statistics

We studied the turbulence around the protuberance formed by one of the borosilicate beads on top of the permeable bed, as shown in the Figure 8(a), by using PIV and an FLS aimed at eight points around that protuberance. The spatial variability can be observed in the two-dimensional time-averaged statistics of Figs 7.

For the measurement points located above the roughness crest (A1, B1, C1), turbulence was spatially homogeneous and of weak intensity. For the measurement points on the roughness crest (A2, B2, C2), the intensity of turbulence was higher and differences between measurements point were visible. Finally, for the lowest level, in the rough layer (A3, C3), there was large spatial variability in turbulence. The average velocity at point C3 was close to 0 and the signal-to-noise ratio was therefore very low, whereas for A3, upstream of the bead, the velocities were higher, with high turbulence intensity relative to the mean velocity. Because Mignot et al. (2009a,b) have previously shown that velocity profile features depend on how the protuberance influenced the flow, we will not go into this topic further. Here, statistical analysis of the turbulence identifies the region where $T_{u'}$ was the largest. Figure 8 − (b) shows how the empirical error in the averaged velocity computation depended on the measurement's duration T. For the flow zones around point C3, we found that $T_{u'}$ had to be as long as 2 s to obtain a relative error lower than 10%. This was the strongest constraint to our continuous scan methodology.

In the configuration tested, and with $T_{u'} \sim 2$ s, the more restrictive condition was given by inequality (5) because the constraint on the bed topography (4) was largely respected: $f \gg 1/T_{u'} = 0.5$ Hz. The maximum velocity required by the MLS to obtain satisfactory continuous scan measurements could thus be estimated using Eq. (5) at $V_{MLS,max} \sim \frac{L_u}{T_{u'}} \sim 2$ mm/s if L_u was approximated by $d_{50}/2 \sim 4$ mm.

3.5.4 Evaluation results

After the scanning velocity was determined using Equation 5, the MLS run was performed by setting $V_{MLS} = 2$ mm/s. Figures 9(a1) and (c1) show the time-averaged velocity and turbulent stress fields at position $Y_m = 25$ mm from the MLS. Figures 9(a2) and (c2) compare the resulting profiles (averaged along the x-direction) using the FLS and MLS procedures, respectively. Figures 9 (b1) and (d1) show the absolute differences observed between the FLS and MLS procedures carried out on the field and on the averaged profiles. Averaged velocity and turbulent stress at laser sheet position Y_m showed good matches between the FLS and MLS procedures.

Error estimates were obtained by subtracting the FLS velocity and *turbulent stress* profiles from those acquired during the MLS experiment at $Y = 25$ mm (see Figs. 9 (b2) and (d2)). Various times T_{MA} were tested and, as observed in Figs 9(e1) and (e2), the smallest errors were obtained for $T_{MA} = 2$ s, which corresponded to the prediction made in Section 3.5.3. If T_{MA} was shorter or longer than 2 s, the error increased.

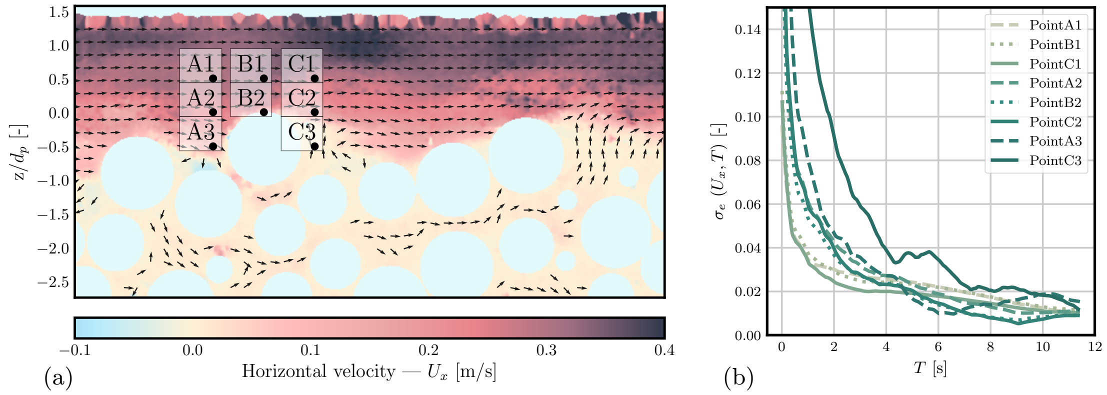

Figure 8: (a) Turbulence in the fluid flows at eight points of interest surrounding a bead on top of the permeable bed were analysed statistically. (b) Evolution of the standard deviation of the empirical error $\sigma_e\ (U_x, t) = \frac{1}{n}\sum_{i=0}^{n}\sqrt{\left((\overline{U_x})_T^i - (\overline{U_x})_{T_{tot}}\right)^2}/(\overline{U_x})_{T_{tot}}$, where $(\overline{U_x})_T^i$ is the average velocity estimated using $n = 700$ samples of duration T against the empirical average calculated over $T_{tot} = 20$ s. The uncertainty is under 10% after 2 s.

4 Repeatability, uniformity and the sidewall

4.1 The sidewall's influence on the flow

To demonstrate the potential of the RIMS method, we present an investigation of the sidewall's influence on the flow. Figure 10 shows a three-dimensional reconstruction of the flow, that is, the horizontal velocity component on the wall of a cuboid that represents the ROI. The fluid's velocity $\overline{u}_x$ increased with y as measurements were made further away from the sidewall. This increase can also be observed in Fig. 11, where $\overline{u}_x$ has been averaged in the x-direction and plotted for different $z'_{\epsilon=0.8}$. We found that the flow region which felt the sidewall's influence least was $Y = 10$ mm away from the wall. This demonstrates that measurements made at less than 5 mm from the wall were strongly affected by it. These observations provide *a posteriori* grounds for using the index matching method, exploring the flow at a sufficient distance from the sidewall and obtaining profiles that can be used to evaluate the different contributions to the double-averaged momentum equation.

Interestingly, in Fig. 11, the velocities close to the free surface ($z'_{\epsilon=0.8} = 9$ mm) and the wall ($Y < 7$ mm) were lower than velocities in deeper positions ($z'_{\epsilon=0.8} = 2$ mm and $z'_{\epsilon=0.8} = 4$ mm) but at the same distance from the wall. This phenomenon can be understood by noting that shear and dispersive turbulence were stronger next to the bed. The resulting mixing processes actively convected momentum from the middle of the flume to the sidewall at these depths, whereas near the free surface, the momentum transfer was of lower magnitude.

4.2 The bed arrangement's influence on reproducibility

When using the PIV–RIMS methodology under similar flow conditions (slope and flow rate) and averaging measurements between $Y = 10$ mm and $Y = 40$ mm (to avoid sidewall influence), consecutive *double-averaged* velocity profiles were similar, thus indicating the experimental procedure's good reproducibility as long as the bed was not rearranged (see Fig. 12).

As the mesoscopic scales (~ 8 cm in the x-direction and ~ 3 cm in the y-direction) used in the double-averaging were not much larger than the bead size ($d_p \sim 1$ cm), our measurements probably suffered from finite size-effects. In other words, we could not guarantee that the porosity and velocity profiles were insensitive to slight changes in the bed arrangement. We now take a closer look at this issue.

Figure 13 compares ten porosity and velocity profiles. These profiles were measured using a constant flow discharge ($q_f = 0.30$ dm^2/s) and varying slopes (1%, 2% and 4%). Initially, the bed was randomly mixed and flattened using a ruler. The flow depth was still $h_s = 5$ cm. The ROI was located at a distance $\delta_g = 90$ cm from the outlet (see Fig. 14). How flow uniformity depended on this value is addressed in the next section. As we had found that slight variations in the slope could affect these profiles, we reset the slope's incline before each run and measured it to within 0.1%.

To compare vertical velocity and porosity profiles, we first needed to fix the origin of the vertical axis. There is no standard procedure for doing this with rough beds. We addressed various possibilities. The roughness crest was unsuitable because it created significant scatter between profiles: at the mesoscopic scale, $z_{\epsilon=0.99}$ was highly influenced by individual grains that were slightly higher than the average bed level. The origin had to

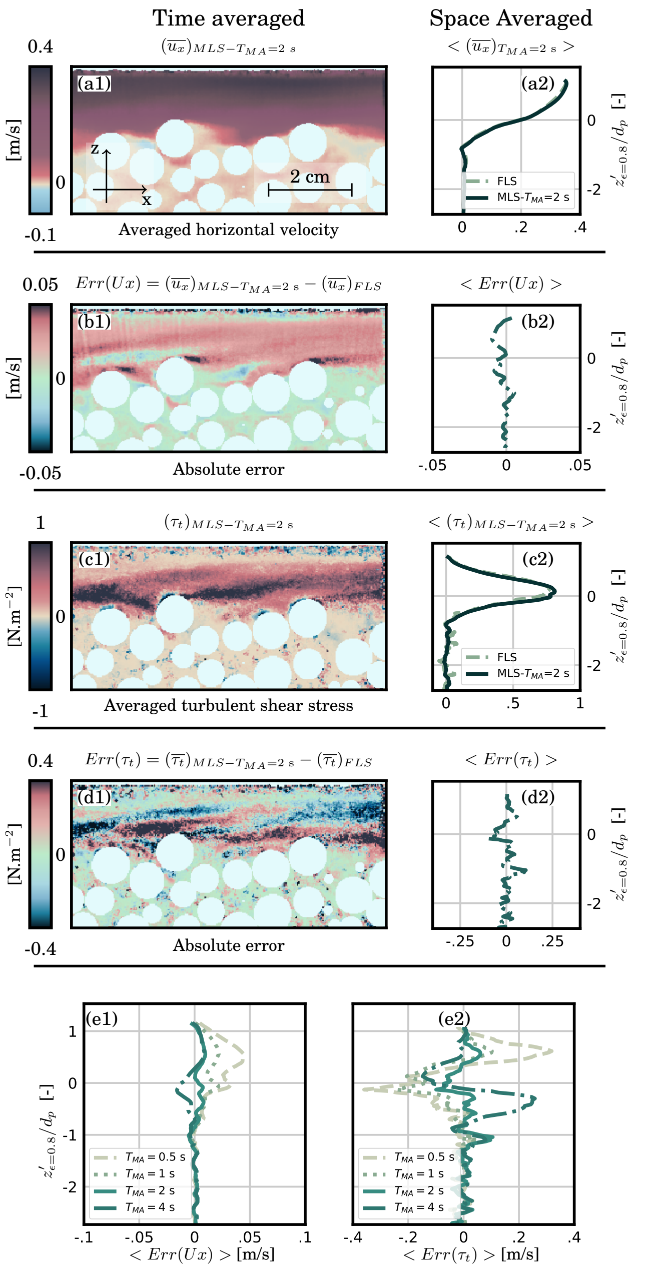

Figure 9: Comparison of estimated profiles at position $Y_m = 25$ mm using the fixed and moving laser sheet methods. The error is thus defined by $Err(\theta) = \langle(\theta)_{MLS-T_{MA}}\rangle_x - \langle(\theta)_{FLS}\rangle_x$, where θ is the velocity profile U_x or the turbulent stress τ_t. T_{MA} is the averaged time or, equivalently, the distance D_{MA} framing the position Y_m. These results show that error is low for both velocity measurements and turbulence statistics when $T_{MA} \sim 2s$.

be fixed at a bed height where the scatter between the porosity profiles was minimal. We found $z_{\epsilon=0.8}$ (see Fig. 13), that is, at $0.3d_p$ below the roughness crest, which was the shift that Voermans et al. (2017) obtained using the porosity inflection method, and which was close to what Nezu and Nakagawa (1993) prescribed. This similarity with the findings described by Voermans et al. (2017) made it possible to compare their results and ours. The Reynolds numbers based on this choice were slightly different to those estimated from the height of the roughness crest, as the flow depth h_f was computed from $z_{\epsilon=0.8}$, which is above $z_{\epsilon=0.99}$.

In the roughness and surface layers, the porosity profiles plotted in Fig. 13 showed a similar pattern from one experiment to another. Slight differences were, however, observed near the roughness crest. Profiles in the subsurface layer (located at $z'_{\epsilon=0.8} < -0.5d_p$ in all runs) showed more scatter. This was the consequence of the ROI's finite size. The porosity profile tended to the packed bed porosity $\epsilon_b \sim 0.4$.

4.3 Uniformity: the influence of the permeable grid

At the flume's upstream end, honeycomb-shaped straighteners stabilised the inflow created by the constant head tank. Downstream of these straighteners, the flow ran over the bi-dispersed borosilicate beads (as shown by Figure 3 – (a)). At the flume outlet, a permeable grid located at x_g let the flow seep out of the bed in such a way that the subsurface flow occupied the bed's entire height (see the enlarged view of the flume in Figure 14). Most experimental investigations of supercritical flows neglect the downstream boundary's influence, but in our experiments involving high bed-permeability, we observed that the downstream boundary condition affected a long section of the flume's length. We thus believe that it is essential to take this influence into account. Indeed, when, for instance, the permeable grid created excessive runoff from the granular bed, the surface flow got into the bed upstream of the grid, causing a decrease in the flow depth over a certain length of the flume δ_g from the grid. The flow depth was then nonuniform over a more or less long part of the flume.

4.3.1 The permeable grid's influence on the subsurface flow

Within the Darcian framework, a quantitative estimation of δ_g^α , i.e. the distance from the grid where the ratio between the estimated surface flow rate and the surface flow rate in a uniform situation, is α is estimated and given in Appendix B

$$\delta_g^\alpha = \left[\frac{q_f - \alpha(q_f - \frac{Kg}{\nu}h_s i)}{\frac{Kg}{\nu}h_s} - i\right]^{-1}(h_s + d_p)/2. \quad (8)$$

With $\nu_{BAE} = 3\times10^{-6}$ m^2/s and $d_p = 8$ mm, permeability was estimated using the Kozeny–Carman equation $K = \frac{\epsilon^3 d_p^2}{180(1-\epsilon)^2} \sim 6.32\times10^{-8}$ m^2. The granular bed depth was set at $h_s = 0.05$ m. With $i = 2\%$ (the experiment's average slope) and $\alpha = 0.8$, we obtained

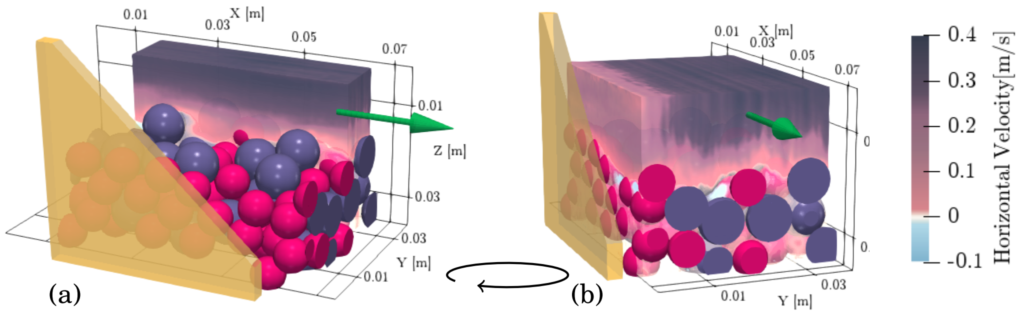

Figure 10: Three-dimensional visualisation of the horizontal velocity. (a) Side view of a slab of the velocity field at FLS position $Y_m = 25$ mm (the same position as the FLS results above—see Fig 7). (b) Frontal view of the flow, sliced along y. This view enables us to appreciate the sidewall's influence. Y is the distance from the sidewall. Z and X are arbitrarily referenced.

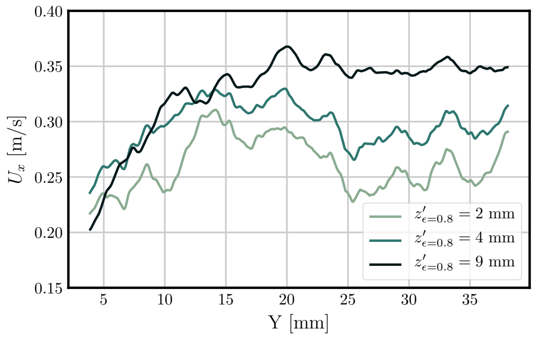

Figure 11: Sidewall influence. The horizontal velocity profile has been averaged along the streamwise x-direction and plotted for different elevations $z'_{\epsilon=0.8} = z - z_{\epsilon=0.8}$ as a function of their distance from the sidewall Y.

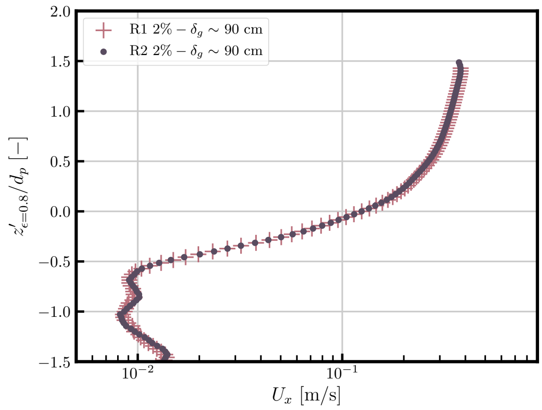

Figure 12: Comparison between two consecutive runs using the PIV–RIMS procedure, with each run using identical bed structure and flow characteristics. The logarithmic scale enables us to visualise the slight scattering in the subsurface layer.

a distance $\delta_g^{0.8} = 0.68$ m. This method predicted that the permeable grid's domain of influence was fairly long relative to the flume length (∼2 m). To control both the subsurface and surface outlet flow rate, we added a buffer medium (BM) with a permeability higher than that of the granular bed at the flume outlet.

4.3.2 Flow uniformity

To verify that the flow was uniform for $x \leq x_g - \delta_g = 90$ cm, we conducted experiments by varying the δ_g length from the outlet. The longest distance was $\delta_g = 110$ cm, and for this value every position along the flume length was within the boundary's domain of influence. The shortest distance was $\delta_g = 60$ cm. Figure 15 shows that the outlet condition affected the flow for δ_g distances as long as 60 cm for $i = 1\%$. Higher velocities were measured in both the surface and subsurface flows, whereas the depth was lower than the averaged velocity profiles at $\delta_g = 90$ cm. This was expected from Eq. 18, where any increase in the subsurface flow rate caused the flow depth to decrease. For $i = 4\%$, differences between profiles could not be statistically attributed to the outlet condition's influence, given the uncertainties and noise induced by the bed arrangement. This analysis suggests that a nearly uniform flow was reached at $\delta_g = 90$ cm because the differences between the profiles at $\delta_g = 110$ cm and $\delta_g = 90$ cm were not statistically significant.

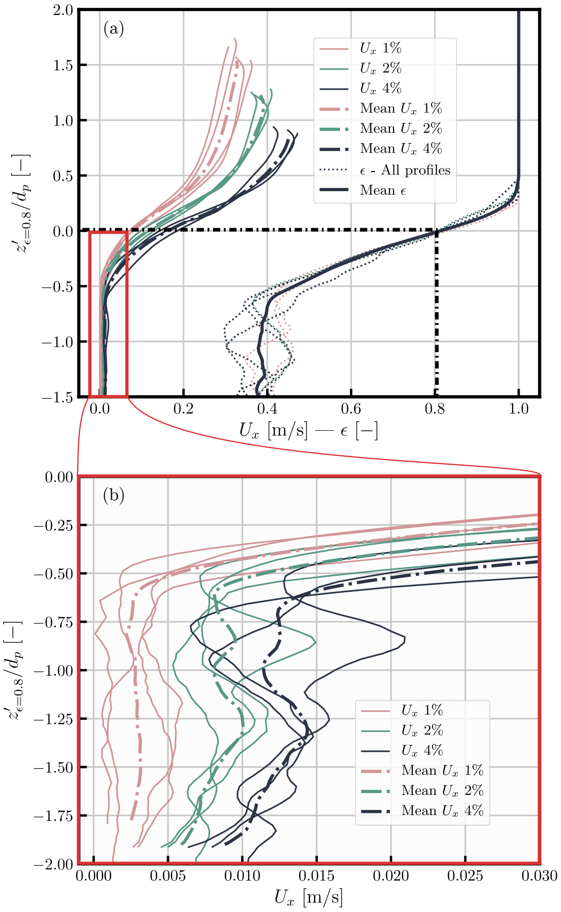

Figure 13: Evaluation of reproducibility with different bed structures. (a) Velocity profiles (continuous and dashed lines) and porosity profiles (dotted lines) for different slopes but using a constant flow discharge $q_f = 0.30 \pm 0.015$ m^2/s. The modified coordinate is given by $z'_{\epsilon=0.8} = z - z_{\epsilon=0.8}$. (b) A zoom in on the roughness and subsurface surface velocities.

5 Preliminary observations based on the PIV–RIMS method

As stated above, the main advantage of the PIV–RIMS methodology is that it averages flow quantities over a thin layer parallel to the bed, as prescribed in the *double-averaging* framework. Figure 13 shows the *smooth* profiles of the flow quantities computed at the mesoscopic scale, similarly to the spatially-averaged porosity profiles.

5.1 Slope and averaged velocities

In the velocity profiles shown in Figure 13 and Figure 15, the slope was increased from 1% to 4%. As the slope was increased, we found that fluid velocities increased in all flow layers, but the U_x increment varied differently according to the layer considered. As the slope was increased from 1% to 4% (see inset of Figure 13), we found that the averaged subsurface layer velocities were multiplied approximately four-fold, whereas free surface velocities were multiplied by 1.5. This difference reflected the various mechanisms at play in those layers: flow through the porous medium was controlled by drag forces, whereas surface flow was mostly driven by the vertical momentum transfered by turbulence. Moreover, (**?**) suggested that all flows involving a sediment–fluid interface exhibit an inflection point in their velocity profiles. This suggestion was confirmed here and is also consistent with the observations by Voermans et al. (2017).

5.1.1 Dispersive and turbulent stresses

Figure 16 shows the dispersive and turbulent stresses obtained using the FLS and PIV–RIMS methodology. One significant difference between the two experimental procedures—use of FLS or MLS—was observable in the measurement of dispersive stresses. The turbulent stresses computed by both procedures showed similar behaviours. Using the FLS, the averaging procedure was done for a single slice at $Y_m = 25$ mm, eliminating the possibility of collecting information at other y positions. Using PIV–RIMS, the laser sheet moved along y and the profiles were averaged over x and y, thus reflecting flow variability in the transverse direction. As observed in previous studies (Voermans et al., 2017; Fang et al., 2018), the dispersive stress exhibited a positive trend at the interface, with maximum dispersive stress located just below the roughness crest (here, at $z'_{\epsilon=0.8} \sim 0$). The turbulent stress maximum was located slightly above the roughness crest, at $z'_{\epsilon=0.8} \sim 0.3d$, and rapidly decreased with decreasing z' (or, equivalently, with increasing porosity).

Turbulent and dispersive stresses rapidly dampened in the subsurface layer, i.e. for depths below $z < z_t$, where bed porosity reached ($z'_{\epsilon=0.8} < -0.5d$ in Figure 16). Flows in the deepest layers were indeed essentially controlled by drag forces on grains. The *roughness layer*, that is, the transition zone where porosity varied sharply from z_{rc} to z_t ($0.3\ d > z'_{\epsilon=0.8} > -0.5\ d$ in Fig. 16), was the zone which presented substantial vertical momentum exchanges. These exchanges resulted from either turbulence or dispersive effects.

6 Concluding remarks

The present article presented a PIV–RIMS technique for measuring averaged flow variables (velocities, stresses and porosity) as part of the *double-averaging* approach. The technique was applied to a turbulent unidirectional flow over a porous, coarse-grained bed. Combining laser scanning and iso-index techniques (RIMS) made it possible to obtain accurate porosity profiles $\epsilon(z)$. Coupled with the PIV processing, this technique

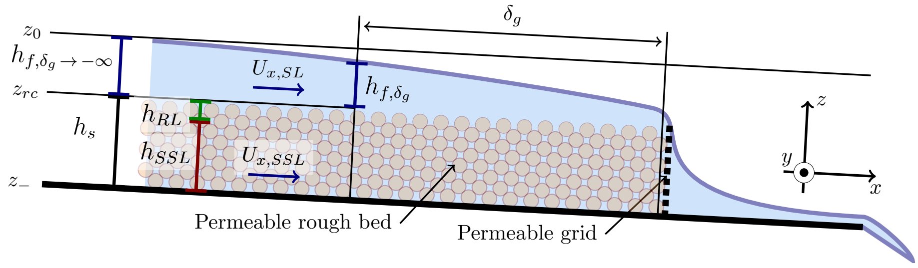

Figure 14: Permeable outlet condition to ensure a subsurface flow. Measurements must be performed along a sufficiently long distance δ_g to ensure that this condition's boundary effect is negligible.

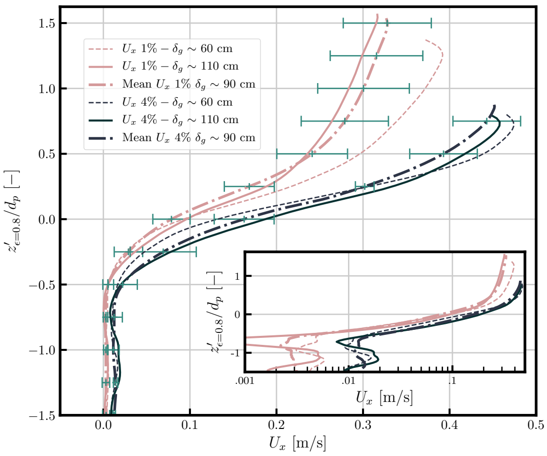

Figure 15: Velocity profiles for various δ_g values with which to evaluate the flow uniformity condition along the flume. The dashed-dotted lines represent the averaged velocity profiles at $\delta_g = 90$ cm. The error bars show the deviations from the averaged profiles due to the modification of the bed structure. They represent the 95% confidence interval. $\sigma_{U_x}(z)$ is the standard deviation at z calculated from the profiles shown in Figure 13. The continuous lines are the profiles measured at $\delta_g = 60$ cm and the dashed lines were measured at $\delta_g = 90$ cm. The bottom-right inset plots the same profiles using a logarithmic scale to emphasise the marked differences at low velocities.

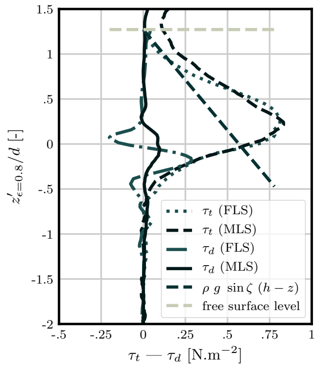

Figure 16: Comparison of the dispersive and turbulent stresses obtained using either a fixed laser sheet (FLS) or the PIV–RIMS methodology. In contrast to using the FLS procedure, PIV–RIMS captures the variability of interactions in the transverse direction y. The resulting averaged profiles provide a better representation of the profiles at the mesoscopic scale.

enabled us to determine the velocities in the surface, roughness and subsurface layers of the fluid.

The PIV–RIMS methodology minimised data storage capacity requirements and experiment duration, but it did require adjustments to the experimental parameters: the velocity of the MLS V_{MLS} had to be slow enough to extract the flow's spatial and temporal variability. To measure mean flow properties far from the flume sidewalls influence, we computed velocity profiles by averaging the flow between $Y = 10$ mm and $Y = 40$ mm.

As the ROI's dimensions were constrained by the flume, measurements were sensitive to bed arrangement between runs. However, reproducibility tests were conducted successfully allowing to measure the slope influence. We also found that we had to place the ROI sufficiently far from the flume outlet—at $\delta_g = 90$ cm—to ensure flow uniformity on average.

Preliminary observations revealed the roughness layer's crucial role in the transfer of vertical momentum. These observations were thus in contrast with the assumption commonly used in most extant models—that there is a discontinuous porosity profile at the bed–flow interface. A valuable alternative might be to consider the roughness layer and model the continuous variations in the velocity and porosity profiles.

The PIV–RIMS methodology opens up another avenue for refining closures involved in current models working at the mesoscopic scale (e.g. models based on double-averaged momentum equations), which should contribute to a better understanding of flow resistance or mass transport in various settings (e.g. mountain rivers).

References

G. S. Beavers and D. D. Joseph. Boundary conditions at a naturally permeable wall. *Journal of fluid mechanics*, 30(1):197–207, 1967.

J.Y. Bouguet. Pyramidal implementation of the affine lucas kanade feature tracker description of the algorithm. *Intel Corporation*, 5(1-10):4, 2001.

A. Boutier. Vélocimétrie laser pour la mécanique des fluides. *Hermes Science-Lavoisier*, 2012.

W.P. Breugem, B.J. Boersma, and R.E. Uittenbogaard. The influence of wall permeability on turbulent channel flow. *Journal of Fluid Mechanics*, 562:35–72, 2006.

H.C. Brinkman. A calculation of the viscous force exerted by a flowing fluid on a dense swarm of particles. *Applied Scientific Research*, 1(1):27–34, 1949.

S. M. Cameron, V. I. Nikora, and M. T. Stewart. Very-large-scale motions in rough-bed open-channel flow. *Journal of Fluid Mechanics*, 814:416–429, 2017.

K.. Chen, Y. Lin, and C. Tu. Densities, viscosities, refractive indexes, and surface tensions for mixtures of ethanol, benzyl acetate, and benzyl alcohol. *Journal of Chemical & Engineering Data*, 57(4):1118–1127, 2012.

H. Fang, X. Han, G. He, and S. Dey. Influence of permeable beds on hydraulically macro-rough flow. *Journal of Fluid Mechanics*, 847:552–590, 2018.

M. Ghisalberti and H. Nepf. The structure of the shear layer in flows over rigid and flexible canopies. *Environmental Fluid Mechanics*, 6(3):277–301, 2006.

Dominique Heitz, Etienne Mémin, and Christoph Schnörr. Variational fluid flow measurements from image sequences: synopsis and perspectives. *Experiments in fluids*, 48(3):369–393, 2010.

C. Kähler, T. Astarita, P. Vlachos, J. Sakakibara, R. Hain, S. Discetti, R. La Foy, and C. Cierpka. Main results of the 4th international PIV challenge. *Experiments in Fluids*, 57(6):97, 2016.

C. Keylock. Flow resistance in natural, turbulent channel flows: The need for a fluvial fluid mechanics. *Water Resources Research*, 51(6):4374–4390, 2015.

T. Liu and L. Shen. Fluid flow and optical flow. *Journal of Fluid Mechanics*, 614:253–291, 2008.

C. Mendoza and D. Zhou. Effects of porous bed on turbulent stream flow above bed. *Journal of Hydraulic Engineering*, 118(9):1222–1240, 1992.

E. Mignot, E. Barthélemy, and D. Hurther. Double-averaging analysis and local flow characterization of near-bed turbulence in gravel-bed channel flows. *Journal of Fluid Mechanics*, 618:279–303, 2009a.

E. Mignot, D. Hurther, and E. Barthélemy. On the structure of shear stress and turbulent kinetic energy flux across the roughness layer of a gravel-bed channel flow. *Journal of Fluid Mechanics*, 638:423–452, 2009b.

M. Miozzi, B. Jacob, and A. Olivieri. Performances of feature tracking in turbulent boundary layer investigation. *Experiments in fluids*, 45(4):765, 2008.

I. Nezu. Open-channel flow turbulence and its research prospect in the 21st century. *Journal of Hydraulic Engineering*, 131(4):229–246, 2005.

I. Nezu and H. Nakagawa. Turbulence in open channels. *IAHR/AIRH Monograph. Balkema, Rotterdam, The Netherlands*, 1993.

I. Nezu and W. Rodi. Open-channel flow measurements with a laser doppler anemometer. *Journal of Hydraulic Engineering*, 112(5):335–355, 1986.

W.-J. Ni and H. Capart. Cross-sectional imaging of refractive-index-matched liquid-granular flows. *Experiments in Fluids*, 56(8):163, 2015.

V. Nikora, D. Goring, I. McEwan, and G. Griffiths. Spatially averaged open-channel flow over rough bed. *Journal of Hydraulic Engineering*, 127(2):123–133, 2001.

V. Nikora, I. McEwan, S. McLean, S. Coleman, D. Pokrajac, and R. Walters. Double-averaging concept for rough-bed open-channel and overland flows: Theoretical background. *Journal of Hydraulic Engineering*, 133(8):873–883, 2007.

J. Ochoa-Tapia and S. Whitaker. Momentum transfer at the boundary between a porous medium and a homogeneous fluid—i. theoretical development. *International Journal of Heat and Mass Transfer*, 38 (14):2635–2646, 1995.

D. Pokrajac and C. Manes. Velocity measurements of a free-surface turbulent flow penetrating a porous medium composed of uniform-size spheres. *Transport in Porous Media*, 78(3):367, Feb 2009. ISSN 1573-1634. doi: 10.1007/s11242-009-9339-8. URL `https://doi.org/10.1007/s11242-009-9339-8`.

M. Rosti, L. Cortelezzi, and M. Quadrio. Direct numerical simulation of turbulent channel flow over porous walls. *Journal of Fluid Mechanics*, 784:396–442, 2015.

Gauthier Rousseau. Turbulent flows over rough permeable beds in mountain rivers: Experimental insights and modeling. Technical report, EPFL, 2019.

F. Scarano and M. Riethmuller. Iterative multigrid approach in piv image processing with discrete window offset. *Experiments in Fluids*, 26(6):513–523, 1999.

J. Shi. Good features to track. In *Computer Vision and Pattern Recognition, 1994. Proceedings CVPR'94., 1994 IEEE Computer Society Conference on*, pages 593–600. IEEE, 1994.

N. Tilton and L. Cortelezzi. Linear stability analysis of pressure-driven flows in channels with porous walls. *Journal of Fluid Mechanics*, 604:411–445, 2008.

K. van der Vaart, P. Gajjar, G. Epely-Chauvin, N. Andreini, J. Gray, and C. Ancey. Underlying asymmetry within particle size segregation. *Physical review letters*, 114(23):238001, 2015.

J. J. Voermans, M. Ghisalberti, and G. N. Ivey. The variation of flow and turbulence across the sediment–water interface. *Journal of Fluid Mechanics*, 824: 413–437, 2017.

G. A. Zampogna and A. Bottaro. Fluid flow over and through a regular bundle of rigid fibres. *Journal of Fluid Mechanics*, 792:5–35, 2016.

G. Zhang and H. Chanson. Application of local optical flow methods to high-velocity free-surface flows: Validation and application to stepped chutes. *Experimental Thermal and Fluid Science*, 90:186–199, 2018.

A Image velocimetry processing

This Appendix details the three principal steps of the image velocimetry algorithm used to yield the velocity field from consecutive images. The test on PIV challenge Case A (Kähler et al., 2016), as well as the internet address needed to access to the algorithm's detail, are provided at the end of this Appendix.

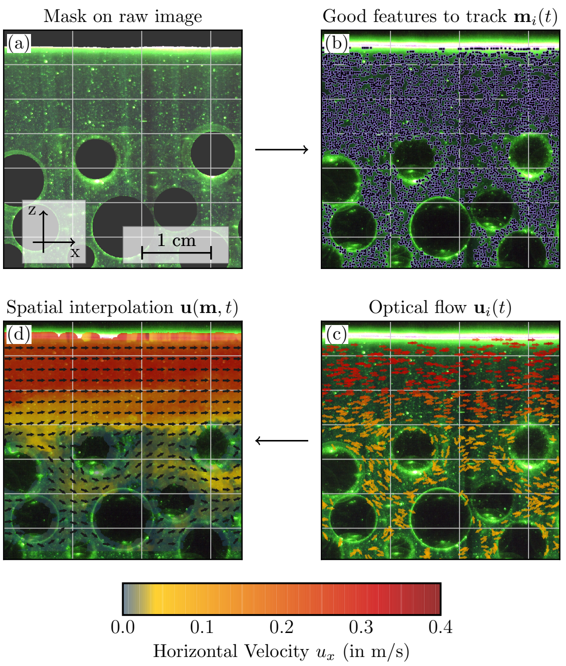

Figure 17: Graphical overview of the workflow: from the raw image to the velocity field.

A.1 Pre-processing

For a given laser sheet position Y_m, a mask is generated from the bead positions to restrict measurement to the interstitial flow zones and the surface flow. Similarly, the fluctuating fluid/air interface is detected in order to mask the upper part of the frame [see Figure 17(a)].

The Contrast-Limited Adaptive Histogram Equalisation (CLAHE) algorithm (grid size = 32×16 px, clip limit = 8) is used to improve image contrast. Hot pixels (with constant high-intensity values) may be present during the recording, as may local and temporary (long duration in comparison with the particle displacement) hot spots due to reflection. To solve this problem, a background removal procedure is performed by subtracting the average frame.

Before any velocity measurements, the *Good Feature to Track* (GFT) algorithm selects features that maintain good contrast, i.e. that are able to provide accurate velocity estimates (Shi, 1994) [see Figure 17(b)]. This pre-selection has two advantages: first, by discarding low-quality points it diminishes errors, and second, it decreases the number of potential interrogation windows, thereby making the algorithm more efficient. Using classic PIV methods, the entire domain is usually computed within regularly spaced interrogation windows and low-quality measurements are generally discarded using post-processing methods. The present study's method avoids processing those zones with a low signal-to-noise ratio. After this step, the points $\mathbf{m}_i = (x, z)_i^T$ are selected and velocimetry processing is launched.

A.2 Velocimetry processing

The velocimetry algorithm measures the local (region-based) *optical flow* by means of a pyramidal implementation of the Lukas–Kanade method (Bouguet, 2001) [see Figure 17(c)]. This method minimises the square of the *Displaced Frame Difference*. To better understand the equations involved in this algorithm and its link to classic PIV, the procedure is detailed below, based on the papers by Heitz et al. (2010) and Liu and Shen (2008).

Given a position $\mathbf{m} = (x, z)^T$ in the image and the intensity function $I(\mathbf{m}, t)$ of the image field, the velocity field is denoted as

$$\mathbf{u}(\mathbf{m}) = (u_x(\mathbf{m}), u_z(\mathbf{m}))^T \tag{9}$$

The Optical Flow Constraint (OFC) equation representing the brightness constancy can be written as

$$\frac{\partial I}{\partial t} = \mathbf{u} \cdot \nabla I \tag{10}$$

Equation 10 is the linear formulation of the matching formula between two consecutive images, and is also known as the *Displaced Frame Difference*:

$$I(\mathbf{m} + \mathbf{d}(\mathbf{m}), t + \delta t) - I(\mathbf{m}, t) = 0 \tag{11}$$

where $\mathbf{d}(\mathbf{m})$ denotes the displacement field between two images. With the Lukas–Kanade method, the displacement field between two consecutive images is determined by minimising the square of the *Displaced Frame Difference* model

$$\mathbf{d}(\mathbf{m}) = \arg\min_{\mathbf{d}} \sum_{\mathbf{r} \in W(\mathbf{m})} (I(\mathbf{r}+\mathbf{d}, t+\delta t) - I(\mathbf{r}, t))^2 \tag{12}$$

where $W(\mathbf{m})$ is the interrogation window around the point of interest. Since $I(\mathbf{m}, t)$ is independent of $\mathbf{d}$, Equation 12 is equivalent to:

$$\mathbf{d}(\mathbf{m}) = \arg\min_{\mathbf{d}} \sum_{\mathbf{r} \in W(\mathbf{m})} I(\mathbf{r}+\mathbf{d}, t+\delta t)^2 - 2I(\mathbf{r}+\mathbf{d}, t+\delta t) I(\mathbf{r}, t) \tag{13}$$

Equation 13 shows that the minimisation of the square of the *Displaced Frame Difference* includes the correlation between two consecutive images. The displacement field estimated using this method is thus equivalent to the displacement field obtained using classic PIV if the quantity $\sum_{\mathbf{r}\in W(\mathbf{m})} I(\mathbf{m}+\mathbf{d}(\mathbf{m}), t+\delta t)^2$ does not depend on $\mathbf{d}$. Classic cross-correlation techniques implicitly use this assumption, but it is locally strengthened when small interrogation windows or large velocity gradients are considered. This is probably why this method works well for the current study problem, where small pore sizes limit the windowing.

The *pyramidal* application of the algorithm aims to increase its dynamic range, i.e. deal with significant pixel motion. The pyramid refers to the successive low-pass filtering and sub-sampling of the image sequence. The levels of the pyramid (1,2,3,...) represent the number of passes and the resolution of the image for the first pass on which the Lukas–Kanade velocimetry method is executed. For example, if the image has a resolution of 400×400 px and the pyramid has two levels, the first image has a resolution of 100×100 px. In this image, the pixel motion is smaller, and the Lukas–Kanade method (with the same window size) measures the overall movement to introduce a shift for the second pass. This methodology is the equivalent of the iterative multi-grid method commonly used in fluid mechanics (Scarano and Riethmuller, 1999). For this experiment, the pyramidal Lukas–Kanade method is parametrised with a 16 × 16 px window and three pyramidal levels.

At the end of this step, the velocity is obtained for each of the selected points $\mathbf{u}_i = (u_x, u_z)_i^T$ [see Figure 17 (c)].

A.3 Post-processing and interpolation scheme

The final step consists of an interpolation process to obtain a velocity field from the isolated points where velocity was known, filling the gaps where the image quality was poor or where the number of seeding particles was too small. This step is commonly performed when using particle tracking velocimetry (PTV) algorithms, but it is computationally expensive. Recent improvements in the Visualisation ToolKit (VTK) library allow use of a tree-like data structure to partition the 2D space and create buckets (methods that are commonly used in 3D graphics or 3D game engines). The search for the points or closer neighbours is then more efficient.

Before the interpolation process, the velocity vectors are subjected to two filters to detect potential outliers. The first filter detects and suppresses isolated points, whereas the second filter detects outliers by making comparisons with the local averaged velocity.

A Gaussian interpolation scheme uses a kernel with a 15 px radius and a standard deviation of 5.6 px. Finally, using this process the velocity field between two images can be reproduced [see Figure 17 (d)].

A.4 Test on the 4th PIV challenge - Case A

An overview of the literature on the application of Lukas–Kanade techniques to fluid mechanics revealed only a few contributions (Miozzi et al., 2008; Zhang and Chanson, 2018). The algorithm developed for this article was performance-tested on the image sequences of the 4th PIV Challenge Case A (Kähler et al., 2016). The resulting velocity measurements (Figure 18 and Figure 19) showed good agreement with the main measurements performed by the twenty leading participants in the 4th PIV Challenge. The main code, termed *opyFlow*, and the algorithms used to provide the figures below, showing the results of the test, have been uploaded to GitHub (`https://github.com/groussea/opyflow`). With regards to the different comments contained in the manuscripts in this domain (e.g. Boutier (2012); Heitz et al. (2010)), this methodology seems more accurate and efficient than traditional PIV methodologies.

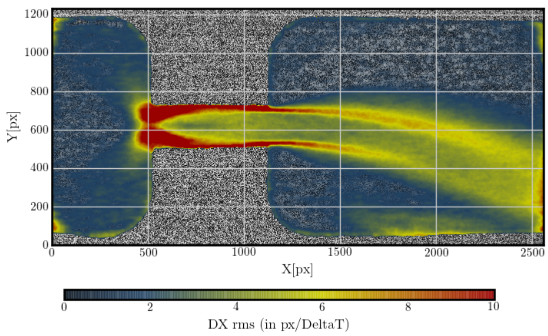

Figure 18: Root mean square of the displacements obtained from our image velocimtery processing on the 4th PIV Challenge - Case A (e.g. Kähler et al. (2016))

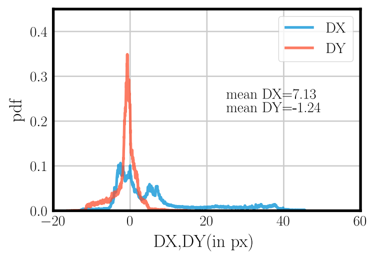

Figure 19: Histogram of the vertical and horizontal displacement measured from our image velocimtery processing on the 4th PIV Challenge - Case A (e.g. Kähler et al. (2016))

B Influence of the permeable grid's distance from the measurement estimated using Darcy's law

This Appendix was developed to obtain a quantitative estimation of δ^{α}, i.e. the distance from the grid where the surface flow is α % of the theoretical surface flow in a uniform situation (see Figure 14). The problem is posed within Darcy's framework.

Let $z_{surf}(\delta_g)$ be the free surface level at distance δ_g. The pressure drop between the constant air pressure on the grid and the fluid pressure at a vertical coordinate z is given by $\Delta P(z) = P_{air} - P(z)$, where $P(z)$ is the static pressure $P(z) = P_{air} + \rho_f g(z_{surf} - z)$.

Thus, the subsurface velocity $U_{SSL}(z)$ at z will be influenced by both the gravity gradient and the pressure drop, and it can be predicted, at first approximation, by:

$$\epsilon U_{x,SSL}(z) = -\frac{K}{\rho_f \nu}\left(\frac{\Delta P(z)}{D_g} + \rho_f g i\right) \tag{14}$$

Within the Darcy framework, the subsurface layer flow is not expected to exhibit linear behaviour at the outlet, where velocities increase. However, the Ergün equation's quadratic term usually decreases the permeability, and the linear approximation has the effect of overestimating the flow inside the porous bed at the outlet.

Thus, the increase of the total subsurface flow discharge $q_{f,h_{SSL}}$ is given as a function of δ_g:

$$q_{f,h_{SSL}}(\delta_g) = \int_0^{h_{SSL}} \frac{Kg}{\nu}\left(\frac{z_{surf}(\delta_g) - z}{\delta_g} + i\right) dz \tag{15}$$

$$= \frac{Kg}{\nu} h_{SSL}\left[\frac{h_f(\delta_g) + h_{RL} + \frac{h_{SSL}}{2}}{\delta_g} + i\right] \tag{16}$$

At this point, it is observed that as $\delta_g \to +\infty$, flow discharge in the bed tends to its expected steady value $q^1_{f,h_s} = \frac{Kg}{\nu} h_s i$ and the steady surface flow is given by $q^1_{f,SL+RL} = q_f - q^1_{f,SSL}$.

Equation 16 involves $h_f(\delta)$ which is non-uniform along x. To resolve this equation, a relation between surface level and subsurface flow discharge must be provided. It is quite complex due to the non-uniformity of both surface velocity and depth. Instead, h_{SL} is supposed to be negligible with respect to $h_{SSL} + h_{RL}$. This assumption seems reasonable since h_f is about 0 at the outlet condition. Also, we must scale h_{RL} and h_{SSL}. As observed experimentally, $h_{RL} \sim d_p$ and the subsurface layer thickness are given by $h_{SSL} \sim h_s - d_p$, where h_s is the initial total sediment depth fixed manually.

The next step produces the distance δg, where the surface flow decrease is negligible. With the condition that $q_{f,SL} > \alpha q^1_{f,SL}$, where α is the quality coefficient (that should be close to one to obtain a nearly uniform flow), we obtain the following equation:

$$q^{\alpha}_{f,SL}(\delta^{\alpha}_g) = q_f - q_{f,h_s}(\delta^{\alpha}_g) \tag{17}$$

$$= q_f - \frac{Kg}{\nu} h_s\left[\frac{h_{RL} + \frac{h_{SSL}}{2}}{\delta^{\alpha}_g} + i\right] = \alpha q^1_{f,SL} \tag{18}$$

The height δ^{α}, above which this condition is verified, is thus provided by:

$$\delta^{\alpha}_g = \left[\frac{q_f - \alpha(q_f - \frac{Kg}{\nu} h_s i)}{\frac{Kg}{\nu} h_s} - i\right]^{-1} (d_p + (h_s - d_p)/2) \tag{19}$$